

**'Flash' annealing in a cold-rolled low carbon steel alloyed with Cr, Mn, Mo, and Nb
Part I - Continuous phase transformations**

Castro Cerda, Felipe Manuel; Vercruyssen, Florian; Goulas, Konstantinos; Schulz, Bernd ; Petrov, Roumen H.

DOI

[10.1002/srin.201800098](https://doi.org/10.1002/srin.201800098)

Publication date

2019

Document Version

Final published version

Published in

Steel Research International

Citation (APA)

Castro Cerda, F. M., Vercruyssen, F., Goulas, K., Schulz, B., & Petrov, R. H. (2019). 'Flash' annealing in a cold-rolled low carbon steel alloyed with Cr, Mn, Mo, and Nb: Part I - Continuous phase transformations. *Steel Research International*, 90(1), Article 1800098. <https://doi.org/10.1002/srin.201800098>

Important note

To cite this publication, please use the final published version (if applicable).
Please check the document version above.

Copyright

Other than for strictly personal use, it is not permitted to download, forward or distribute the text or part of it, without the consent of the author(s) and/or copyright holder(s), unless the work is under an open content license such as Creative Commons.

Takedown policy

Please contact us and provide details if you believe this document breaches copyrights.
We will remove access to the work immediately and investigate your claim.



'Flash' Annealing in a Cold-Rolled Low Carbon Steel Alloyed With Cr, Mn, Mo, and Nb: Part I - Continuous Phase Transformations

Felipe Manuel Castro Cerda,* Florian Vercruyse, Constantinos Goulas, Bernd Schulz, and Roumen H. Petrov

The aim of the present work is to study the microstructure evolution of a cold-rolled low carbon steel alloyed with Cr, Mn, Mo, and Nb during continuous heating. The formation of austenite and its further transformation is examined by means of peak annealing experiments at three different heating rates, followed by quenching. The effect of carbide-forming alloying elements in the kinetics of austenite formation and decomposition is discussed with the aim of DICTRA calculations. Electron Probe Micro Analysis allows the detection of small compositional fluctuations within the microstructure, which are responsible for local changes in the mechanism of austenite formation. It is experimentally demonstrated that the temperature dependence of the austenite fraction is relatively insensitive to the heating rate. It is suggested that carbide-forming alloying elements slow down the kinetics of austenite formation.

discussed by Gridnev and Trefilov.^[7] Of particular interest is the finding that the austenite transformation in a hypereutectoid steel with initial martensitic microstructure happens in martensitic (diffusionless) mechanism at heating rates above $3500^{\circ}\text{C s}^{-1}$. The anisothermal formation of austenite was kinetically described for different initial microstructures by Rödel and Spies^[8] (ferrite-cementite) and Enomoto and Hayashi^[9] (martensite). However, neither of these theoretical studies clearly defines the transition temperatures nor provide experimental evidence of such. Recent studies on austenite formation in low and medium carbon steel with ferrite-pearlite^[10] and ferrite-spheroidized cementite initial microstructure^[11] offered new experimental evidences, as well as a thermodynamic and kinetic

1. Introduction

The effect of the heating rate on the microstructure of steel has been subject of a number of experimental studies in the past decades.^[1–5] There, it was acknowledged that austenite transformation undergoes a transition from carbon diffusion controlled to a massive mechanism when heating rate exceeds certain levels.^[6] The initial microstructure plays a major role on the mechanism and kinetics of austenite formation, as early

description of the transition of austenite formation mechanisms from carbon diffusion controlled to a massive mechanism. However, these studies lack of local compositional analysis and the effect of segregation of alloying elements was not experimentally demonstrated.

In the present study, the goal is to evaluate the effect of the heating rate on the microstructure of a low carbon steel alloyed with Cr, Mn, Mo, and Nb. The impact of carbide-forming alloying elements on austenite formation is discussed with the aim of DICTRA calculations. The recently proposed^[10] definition of the transition from diffusion controlled mechanism to massive formation of austenite A_m is evaluated by combined local composition Electron Probe Micro Analysis (EPMA) measurements, and thermodynamic calculations.

2. Experimental Section

2.1. Material and Heat Treatments

The chemical composition of the steel is shown in **Table 1**. The 1.5 mm thick steel sheets were received in the 50% cold-rolled condition and specimens for heat treatment were cut from this material. Controlled-heating experiments at 10, 400, and $1000^{\circ}\text{C s}^{-1}$ were performed on $120 \times 10 \times 1.5$ mm³ specimens in a Gleeble 3800 thermomechanical simulator; the longest axis

Dr. F. M. Castro Cerda, Dr. B. J. Schulz
Department of Metallurgy
University of Santiago de Chile
Alameda Libertador Bdo. O'Higgins 3363, Estación Central, 9170022,
Santiago, Chile
E-mail: felipe.castro@usach.cl

F. Vercruyse, Dr. R. H. Petrov
Department of Electrical Energy
Metals, Mechanical constructions & Systems
Ghent University
Technologiepark 903, 9052 Gent, Belgium

Dr. C. Goulas, Dr. R. H. Petrov
Department of Materials Science and Engineering
Delft University of Technology
Mekelweg 2, 2628CD Delft, The Netherlands

The ORCID identification number(s) for the author(s) of this article can be found under <https://doi.org/10.1002/srin.201800098>.

DOI: 10.1002/srin.201800098

Table 1. Chemical composition (in wt%).

C	Mn	Si	Cr	Mo	Nb	Fe
0.11	1.87	0.03	0.45	0.18	0.03	Rest

of each sample was kept parallel to the rolling direction (RD) of the cold-rolled sheet. The recorded time-temperature curves for each condition is shown in **Figure 1**. Dilatometry experiments at $10\text{ }^{\circ}\text{C s}^{-1}$ were carried out in a Bähr 805A Quench dilatometer, on the samples with size of $10 \times 5 \times 1.5\text{ mm}^3$. In both equipments, the temperature was controlled by an S-type thermocouple spot welded to the midsection of each test sample. Specimens subjected to peak-annealing experiments were heated at various rates (10, 400, and $1000\text{ }^{\circ}\text{C s}^{-1}$) to pre-defined temperatures, held at these temperatures for $<0.3\text{ s}$, and subsequently quenched (with quenching rates of $-150\text{ }^{\circ}\text{C s}^{-1}$). **Table 2** shows the average heating rates and peak temperatures employed in these experiments.

2.2. Characterization

The microstructural evolution of the samples was evaluated via Optical Microscopy (OM), and Scanning Electron Microscopy (SEM). Samples were cut from each heat-treated specimen. The zone of homogeneous microstructure in each specimen was determined by plotting the Vickers hardness (HV3) as a function of distance along the TD plane (i.e., the plane perpendicular to TD). Subsequent characterization and data collection was performed within the limits of the homogeneous zone. Samples taken from each tested specimen were prepared, in accordance with standard procedure, by grinding and polishing to a mirror-like finish using a $1\text{ }\mu\text{m}$ diamond paste, and etching to reveal the microstructure. The polished surface was swabbed in a solution of 4% v/v HNO_3 in ethanol (Nital 4%) for $\approx 4\text{ s}$. Electron backscatter diffraction (EBSD) measurements were performed

Table 2. Summary of average heating rates and peak temperatures applied to the steel samples.

Heating rate, $^{\circ}\text{C s}^{-1}$	Peak temperature, $^{\circ}\text{C}$		
10	771	791	826
400	781	803	841
1000	764	783	824

on a FEI QuantaTM 450-FEG-SEM operated under the following conditions: accelerating voltage: 20 kV, beam current: corresponding to an FEI spot size of 5, aperture size: $30\text{ }\mu\text{m}$, working distance: 16 mm. The sample was tilted by 70° toward the EBSD detector, and the resulting (EBSD) patterns were acquired on a hexagonal scan grid by a Hikari detector operated with EDAX-TSL-OIM-Data Collection version 6 software. Scans were performed at a step size of $0.3\text{ }\mu\text{m}$. The corresponding orientation data were post-processed with EDAX-TSL-OIM-Data Analysis version 7 software using the following grain definition: misorientation with neighboring grains: $>5^{\circ}$, minimum number of points per grain: four, and confident index (CI): >0.1 .

2.3. Electron Probe Micro Analysis Measurements

Electron Probe Micro Analysis (EPMA) measurements were performed with a JEOL JXA 8900R microprobe operated at 10 keV, with nominal beam current 100 nA, employing Wavelength Dispersive Spectrometry (WDS). The beam was focused to reduce the analysis spot diameter, which was approximately $0.2\text{ }\mu\text{m}$. The composition at each analysed location of the sample was determined using the X-ray intensities of the constituent elements after background correction relative to the corresponding intensities of reference materials. The obtained intensity ratios were processed with a matrix correction program CITZAF.^[12] The points of analysis were located on a line across the normal direction of the specimen. The blue line in **Figure 2**

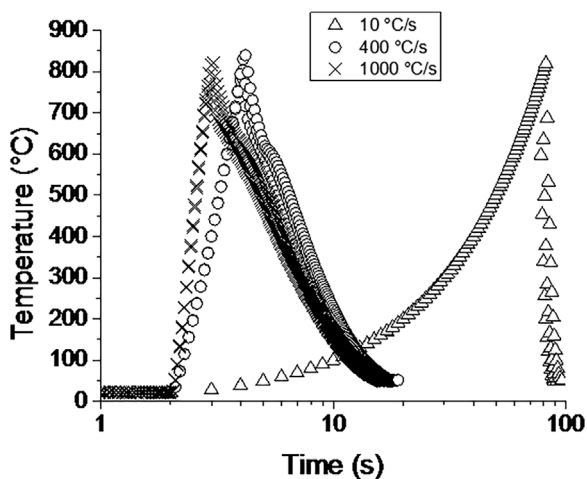


Figure 1. Thermal cycles for samples treated in the Gleeble thermomechanical simulator.

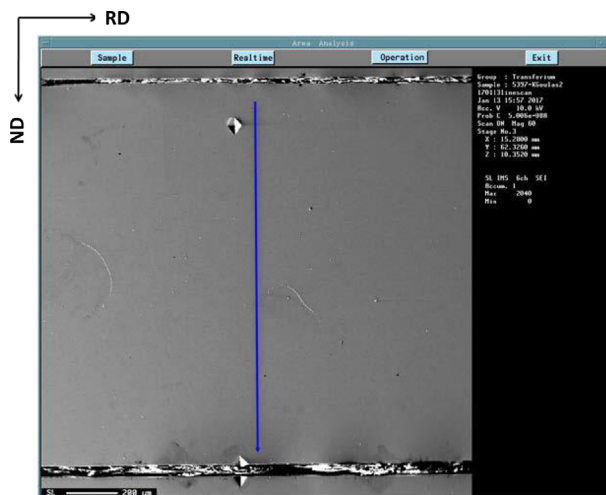


Figure 2. SEM image showing the location of the EPMA in the sample. Scale bar $200\text{ }\mu\text{m}$.

Table 3. Critical temperatures (°C) calculated with ThermoCalc using the information in Table 1.

A_1	A_3	A_m
673	810	837

shows the line scan. The measurements were performed at distance increments of 2 μm and involved the elements Si, Cr, Mn, and Mo, with Fe computed by the difference.

3. Data Post-Processing and Analysis

The phase fractions generated during the anisothermal dilatometric heat treatments are typically estimated via the lever rule. However, this approach yields significant deviations from actual values, owing to the difference in density of pearlite and ferrite.^[13–16] Therefore, in the present study, a correction^[15] was applied to the austenite phase fractions calculated from the dilatometric data. The EBSD scans were taken at a distance of one third of the sample thickness. The raw EBSD data were post-processed (cleaned) to re-assign the incorrectly indexed points using the grain confidence index standardization procedure. The grains were defined as the arrangement of at least 4 points with a misorientation angle smaller than 5° and a confidence index > 0.1. The volume fraction of austenite (martensite) estimated from EBSD measurements was carried out using the Grain Average Image Quality (GAIQ) criteria described elsewhere.^[17]

Thermodynamic calculations were performed using the software ThermoCalc. The calculations were carried out in order to determine the stability of the equilibrium phases observed in the microstructure. Despite that ultrafast heating produces well-known equilibrium deviations in austenite formation,^[6] the hypothesis of local equilibrium^[18] (LE) at the interface is accepted by the present authors and applied to the description of austenite formation.^[10] Table 3 shows the critical temperatures of the steel. A simulation of cementite decomposition on heating at the three heating rates was carried out using the software DICTRA. The general description of the software and the models can be found elsewhere.^[19–21] It was considered a spherical initial volume (cf. Figure 3) consisting of cementite and ferrite, where r_θ : radius of cementite (μm), r_γ : radius of cementite plus austenite (μm), and f_θ : volume fraction of cementite (cf.

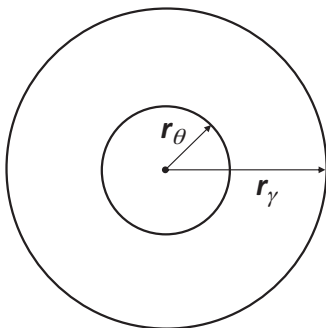


Figure 3. Scheme of the initial volume used to simulate the dissolution of cementite and carbon distribution in austenite.

Table 4. Parameters introduced in Dictra calculations.

r_θ , μm	r_γ , μm	f_θ
0.2	0.85	0.013

Table 4). For the simulation of cementite dissolution, it was considered that all the ferrite was instantaneously transformed into austenite above A_1 .

4. Results

4.1. Initial Microstructure

The initial microstructure is shown in Figure 4. A homogeneous mixture of deformed ferritic (light gray zones in Figure 4a) grains and bainite or fine pearlite (dark gray zones in Figure 4a) is observed. SEM analysis (Figure 4b) revealed the presence fine pearlite, and carbides (C) in the initial microstructure. The initial microstructure does not show a marked banding.

4.2. Microstructure after Heat Treatments

The optical micrographs of the microstructure after heat treatments are displayed in Figure 5. Figure 5a–c show the microstructure of samples heated at 10 °C s⁻¹ (conventional heating rate), whereas Figure 5d–i show samples heated at 400 and 1000 °C s⁻¹ (ultrafast heating rates), respectively. The peak annealing temperature is shown on the upper left corner of each micrograph. The microstructure after heat treatments consists of a mixture of ferrite and martensite. The microstructure of samples heated at 10 °C s⁻¹ (cf. Figure 5a–c) show a significant fraction of recrystallized ferrite. In contrast, samples heated at 400 °C s⁻¹ (cf. Figure 5d–f) and 1000 °C s⁻¹ (cf. Figure 5g–i) only reveal a change in the microstructure of ferrite in samples heated above 803 °C (compared to cold-rolled in Figure 4a). The distribution of martensite (former austenite) is modified from band-like (cf. Figure 5d,g,h) to grain-boundary distribution. This change in the distribution of martensite might be related to the ferrite recrystallization and the change of austenite formation mechanism, and will be further discussed in Section 5.2. A noticeably structure-refining effect accompanies the change in martensite distribution in samples heated at 400 and 1000 °C s⁻¹ above 803 °C (cf. Figure 5e,f,i).

The constitution of the microstructure is revealed in more detail in Figure 6. It should be noticed that the microstructure is consistent with the observations in previous works.^[10,22,23] The ferrite is not completely recrystallized in samples heated below 791 °C. The dark gray areas, initially associated to martensite in optical micrographs in Figure 5, are composed of a mixture of martensite, bainite, partially decomposed pearlite, and cementite (cf. center of Figure 6e). Partially decomposed pearlite is the one in which cementite is partially spheroidized (cf. Figure 6d,e).

The variation of austenite (martensite) fraction with temperature is shown in Figure 7. The solid curve represents the equilibrium fraction calculated with ThermoCalc (database TCFE7). The dotted black curve show the austenite fraction

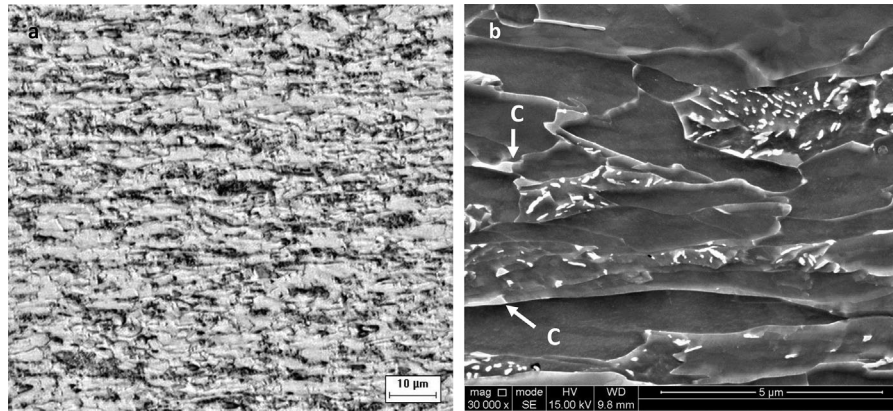


Figure 4. Microstructure of the cold-rolled steel. a) and b) are respectively optical and scanning electron micrographs. C represents cementite.

obtained from dilatometry. The triangles, circles and crosses show EBSD data of samples heated at 10, 400, and 1000 °C s⁻¹, respectively. The blue and red dashed curves show the A_m temperature, as defined in a previous work,^[10] calculated for the average (cf. Table 1) and local (EPMA) chemical compositions, respectively. Phase quantification does not reveal a marked variation of the martensite fraction as a function of the temperature in samples heated at 400 and 1000 °C s⁻¹. The small variation of martensite fraction is also observed in Figure 5d–i. The most significant differences are measured above ≈803 °C and will be further commented in Section 5.

5. Discussion

5.1. Diffusion-Controlled Formation of Austenite

5.1.1. Nucleation

The nucleation of austenite was observed at ferrite/pearlite and ferrite/ferrite boundaries. Evidence of the former is shown in Figure 6d (‘c’ arrow) and the latter in Figure 6a and g (‘M’ arrows). This is consistent with observations of austenite nucleation in steels with ferrite-pearlite initial microstructure.^[10] Although it was shown that the austenite nucleation at the a/θ interface is the most occurring, under UFH rates it is common to find austenite nucleation at a/a boundaries.^[23] It has been shown^[24] that the nucleation of ferrite on γ/γ boundaries occurs with double K-S orientation relationship (OR). Hence, it can be expected that austenite nucleation in a/a boundaries might as well require the same OR. The observation of nucleation of austenite at the a/a interface necessarily suggest a mechanism involving carbon diffusion. Otherwise, a nucleus formed under diffusionless mechanism would have been most likely transformed into massive ferrite upon cooling, thus being undetectable by metallographic observation. The initial microstructure shows grain-boundary cementite (cf. upper left hand side in Figure 4b), which suggest that what it is observed as a/a interface nucleation of austenite might actually correspond to nucleation at a/θ interface. Conversely, in-situ synchrotron measurements^[25] suggest the hypothesis of diffusionless nucleation of austenite during heating.

5.1.2. Growth

The A_m temperature has been previously defined^[10] as the temperature for which $\Delta G^{a-\gamma} = 0$ when $X_C \rightarrow 0$, where $\Delta G^{a-\gamma}$: Gibbs free energy change of the austenite formation from ferrite and X_C : mole fraction of carbon. It represents the temperature at which the austenite formation mechanism change from carbon-diffusion controlled to massive upon heating. Therefore, the fraction of austenite measured below A_m is formed under carbon diffusion. Data measured in Figure 7 show no significant differences between the austenite phase fraction of samples at the three heating rates. It is, thus, reasonable to expect that the kinetics of austenite formation does not show significant difference either. The velocity $v^{\gamma/a}$ of the γ/a interface moving towards proeutectoid ferrite has been defined in ref.^[10] as

$$v^{\gamma/a} = \frac{D_C^\gamma (X_C^\gamma - X_C^{\gamma/a})}{L (X_C^{\gamma/a} - X_C^{a/\gamma})} \quad (1)$$

where $X_i^{k/m}$: mole fraction of element i in phase k at the k/m interface, D_i^k : diffusion coefficient of element i in phase k , and L : considered the effective diffusion distance in austenite. Similarly, one can construct a simplified expression for the diffusion-controlled advance of the γ/θ interface based on a mass-balance at the moving boundary.^[26] This yields

$$v^{\gamma/\theta} = \frac{D_C^\gamma (X_C^{\gamma/\theta} - X_C^{\gamma/a})}{L_p' (X_C^\theta - X_C^{\gamma/\theta})} \quad (2)$$

where L_p' : one-half of the distance between cementite particles. In the Fe–C system, it should be expected that the dissolution of cementite is significantly faster than the full austenite formation, given that $(X_C^\gamma - X_C^{\gamma/a}) < (X_C^{\gamma/\theta} - X_C^{\gamma/a})$ and $L \cdot (X_C^{\gamma/a} - X_C^{a/\gamma}) \gg L_p' \cdot (X_C^\theta - X_C^{\gamma/\theta})$. One could expect that the factor $(X_C^\gamma - X_C^{\gamma/a})$ in Equation (1) will show the largest variation with heating rate, due to the fact that X_C^γ will depend on the fraction of cementite dissolved in austenite. At conventional heating rates, the factor $(X_C^\gamma - X_C^{\gamma/a}) \rightarrow 0$ because the cementite dissolution is faster than the formation of austenite and the carbon will

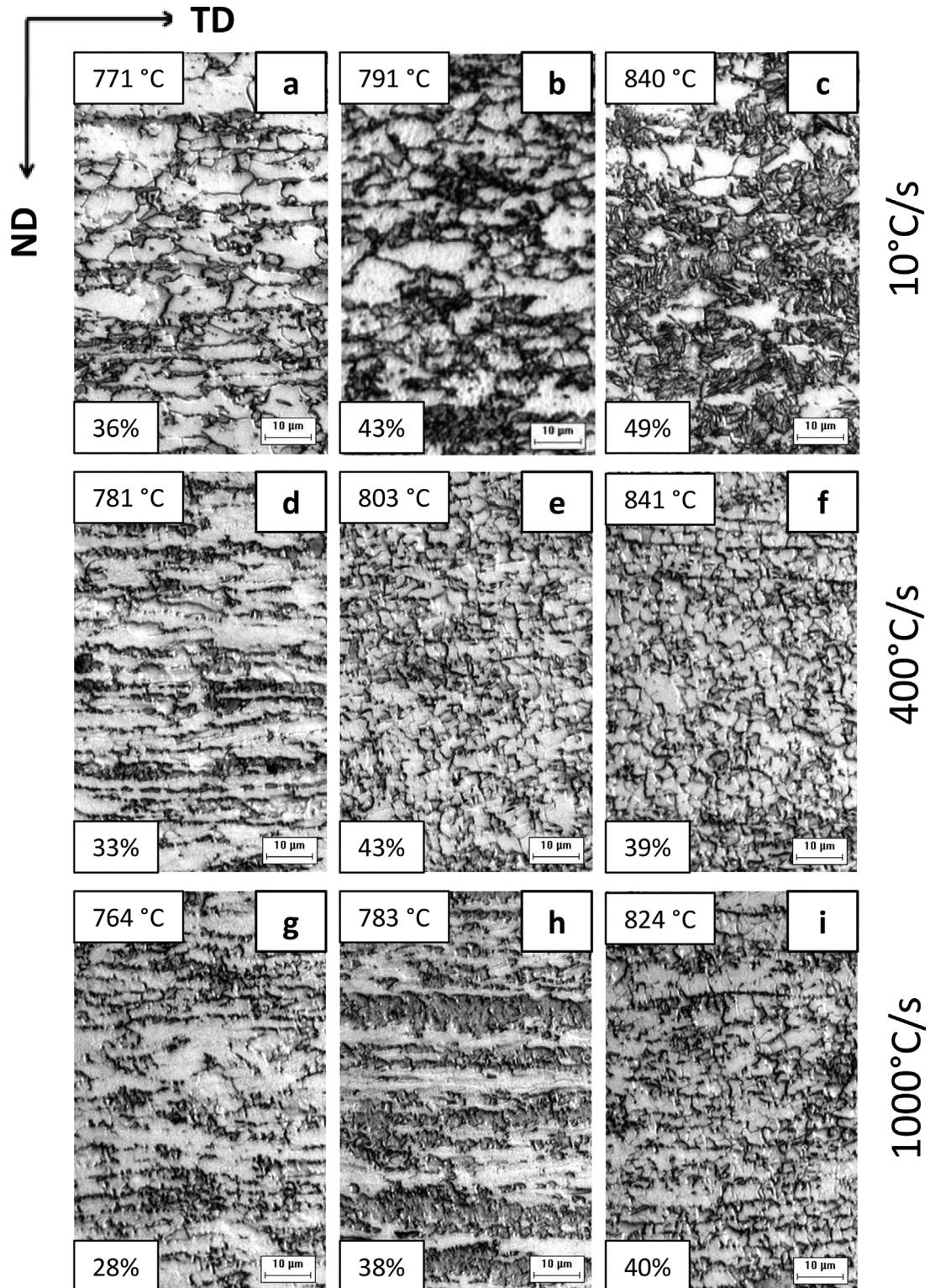


Figure 5. OM of samples heated at $10\text{ }^{\circ}\text{C s}^{-1}$ (a–c), $400\text{ }^{\circ}\text{C s}^{-1}$ (d–f), and $1000\text{ }^{\circ}\text{C s}^{-1}$ (g–i) to different peak temperatures, as indicated in each micrograph. The fraction of martensite is indicated in the lower left corner of each image. Etched with Nital 4%. Scale bar $10\text{ }\mu\text{m}$.

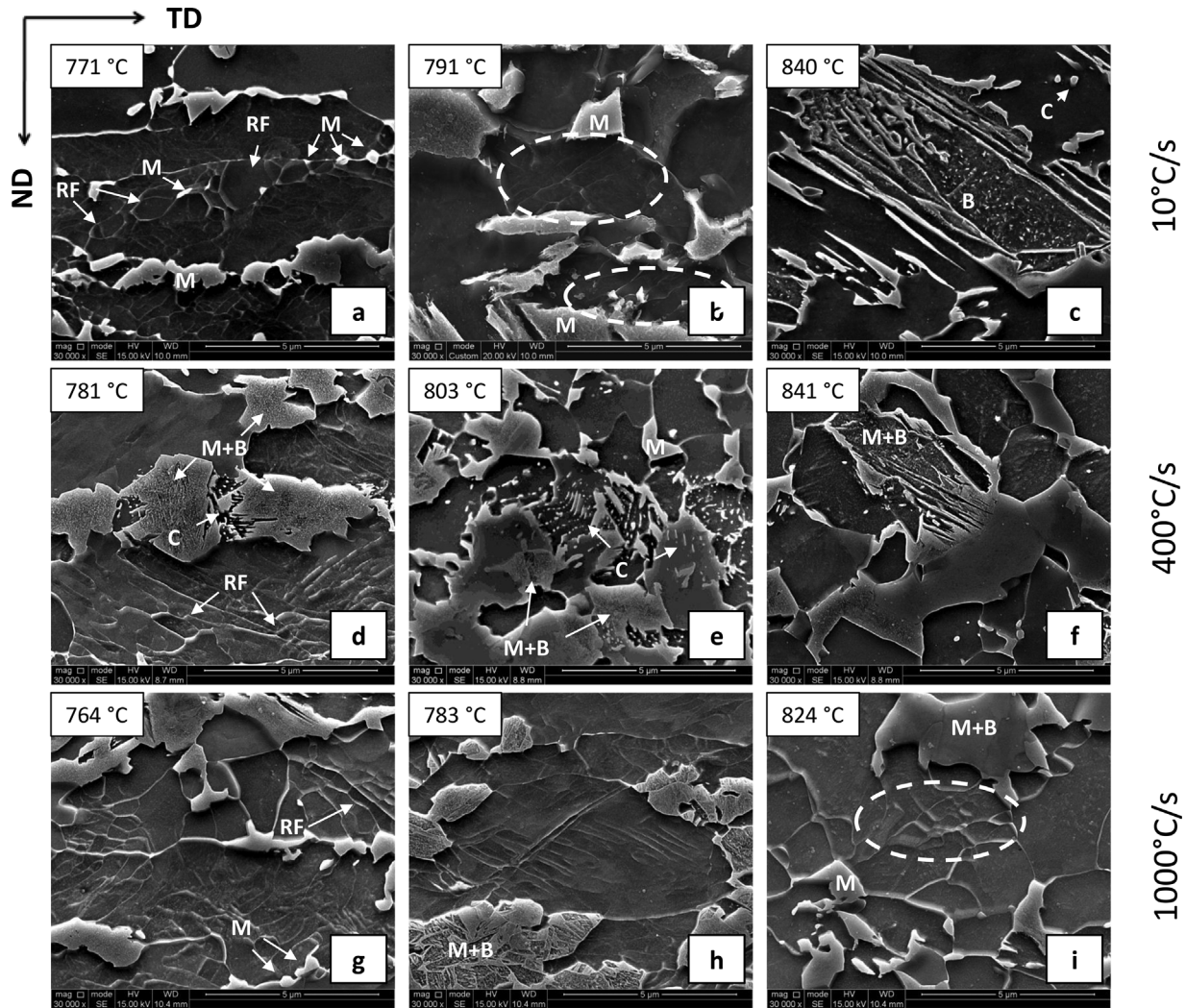


Figure 6. SEM of samples heated at $10^{\circ}\text{C s}^{-1}$ a–c), $400^{\circ}\text{C s}^{-1}$ d–f), and $1000^{\circ}\text{C s}^{-1}$ g–i) to different peak temperatures, as indicated in each micrograph. Etched with Nital 4%. B, M, C, RF indicate bainite, martensite, cementite, and recrystallized ferrite, respectively. Scale bar 5 μm .

homogenize along L . At ultrafast heating rates, it is reasonable to expect that $(X_C^{\gamma} - X_C^{\gamma/a}) \rightarrow (X_C^{\theta/\gamma} - X_C^{\gamma/a})$ because of the reduced time for diffusion and the slower dissolution of cementite.

It has been shown elsewhere^[27] that in Fe–C–M systems, with M being carbide-forming substitutional alloying element as Cr or Mo, the rate of cementite dissolution will be markedly affected by the diffusion of M. One could therefore expect that the factor $(X_C^{\gamma} - X_C^{\gamma/a}) \rightarrow (X_C^{\theta/\gamma} - X_C^{\gamma/a})$ in Equation (1), even at conventional heating rates, hence enabling $v^{\gamma/a}$ comparable to ultrafast heating rates and explaining the similar phase fractions measured in Figure 7.

5.2. Massive Formation of Austenite

Having proposed that; 1) the kinetics of austenite formation is sensitive to the dissolution of cementite and 2) marked kinetic differences in the range of $10\text{--}1000^{\circ}\text{C s}^{-1}$ should not be

expected, it is thus straightforward to realize that the last stage of austenite formation was accomplished by the massive mechanism in samples heated at the three heating rates. The dilatometric curve of $10^{\circ}\text{C s}^{-1}$ (dashed black line in Figure 6) indicates that the transition from diffusion-controlled to massive formation of austenite is smooth. This was already predicted^[23] in previous studies of austenite formation under ultrafast heating and discussed in the framework of the mixed-mode model.^[10] The fraction of martensite above A_m showed in Figure 6 should not be directly associated to the fraction of austenite formed on heating. The metallographic data from samples heated above A_m show the expected discrepancies with respect to the actual austenite fraction, as consequence of the massive formation of ferrite on cooling. The magnitude of the discrepancies are related to the fraction of austenite (and subsequent ferrite) formed massively and therefore it is reasonable to find larger deviations at ultrafast heating rates (cf. circles and crosses above A_m in Figure 6), compared to conventional (cf. triangles above A_m in Figure 6).

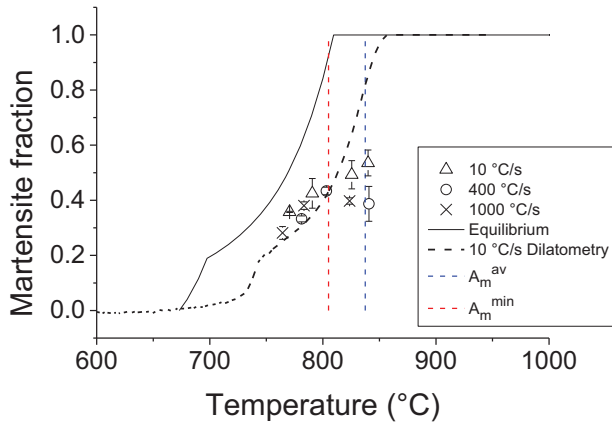


Figure 7. Temperature dependence of the austenite (martensite) fraction. The solid and dashed black lines represent the equilibrium and 10 °C s⁻¹ dilatometry fractions of austenite, respectively. Triangles, circles and crosses show the austenite (martensite) fraction measured by EBSD. The blue and red dashed lines show the A_m temperature, as defined in a previous work,^[10] calculated for the average (cf. Table 1) and local chemical compositions, respectively.

The transition temperature A_m depends on the chemical composition at the γ/α moving boundary. In homogeneous materials, a good approximation to the actual A_m can be obtained from the average chemical composition.^[10] However, micro segregation is always found in low alloy steels and such local chemical fluctuations will affect the A_m temperature. **Figure 8a** shows the local variations of selected elements (mass fractions of Cr, Mn, and Mo in logarithmic scale) across the thickness of the plate (cf. Figure 3). Note that there are significant fluctuations in Mn content. The distribution of Cr and Mo are more homogeneous. One could calculate the corresponding A_m for each point, which is shown in **Figure 8b**. The fluctuations in the onset of massive formation are widely dispersed between the calculated A_3 and the average A_m (calculated from data in Table 1, A_m^{av}).

The minimum value of A_m (corresponding to the maximum segregation) calculated with the data in **Figure 8b** is ~ 815 °C. This value will from now on be denominated as A_m^{min} . Although the local chemical analysis considers a rather small area (approximately 0.2 μm in diameter), it is possible that carbides might have been included in some of the points. Therefore, the compositional variations should be regarded as an average of the ferrite and some carbides. Nonetheless, for calculation purposes it was considered that the composition versus distance data in **Figure 8a** correspond to ferrite composition.

The data in **Figure 6** can be rationalized in the light of the calculated A_m^{min} value (dashed red line). A somewhat better fit to the dilatometric curve is found in data below A_m^{min} temperature, and more significant deviations were measured above A_m^{min} . It leads to the suggestion that a considerable fraction of austenite is formed massively above A_m^{min} . As mentioned in the Section 4.2, a noticeable change in the microstructure is observed above 803 °C in samples heated at 400 and 1000 °C s⁻¹ (cf. **Figure 4e,f, i**), which is believed to be a consequence of the change in the mechanism of austenite formation upon heating. **Figure 9** also shows EBSD evidence of the massive formation of austenite

above A_m^{min} . **Figure 9a-i** show data of samples heated at 10 °C s⁻¹ to 840 °C, 400 °C s⁻¹ to 803 °C, and 1000 °C s⁻¹ to 824 °C, respectively. The dashed area in **Figure 9d-f** show an unusual localization of what seems to be highly-distorted ferrite aligned almost parallel to the longest axis of the grain. The KAM map (cf. **Figure 9e**) confirms that the misorientation at the center, where such distortion is located, is higher than in the outer part of the grain. IPF map (cf. **Figure 9f**) indicates that high and low-distortion regions within the dashed area correspond to a single ferritic grain. It is believed that this ferrite sub-structure, hereby reported for the first time to the knowledge of the authors, is the outcome of the partial massive formation of austenite into a non-recrystallized (deformed) ferritic grain and its further massive transformation into ferrite on cooling. Metallographic evidence of the massive formation of austenite under ultrafast heating rates and subsequent massive transformation of ferrite upon quenching has been recently reported elsewhere,^[10] and show consistency with the present observations.

It can be argued that the morphology of ferrite in the dashed area in **Figure 9d-f** is product of Grain Boundary (GB) nucleation of recrystallized ferrite which stops before

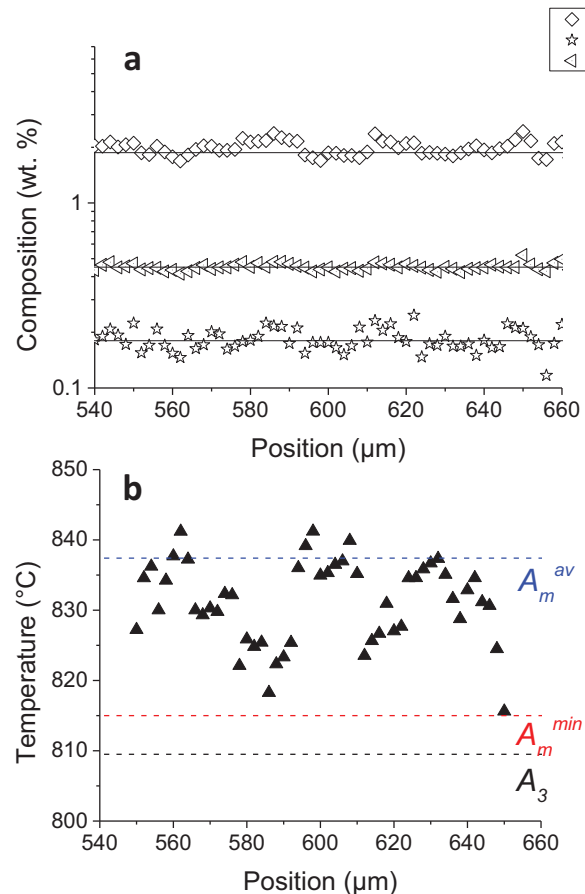


Figure 8. a) Composition (log scale) versus distance profiles for Cr, Mn, and Mo measured by EPMA. The solid lines show the corresponding average values measured by optical spectroscopy. b) Calculated variation of A_m (triangles) as function of the local chemical composition.

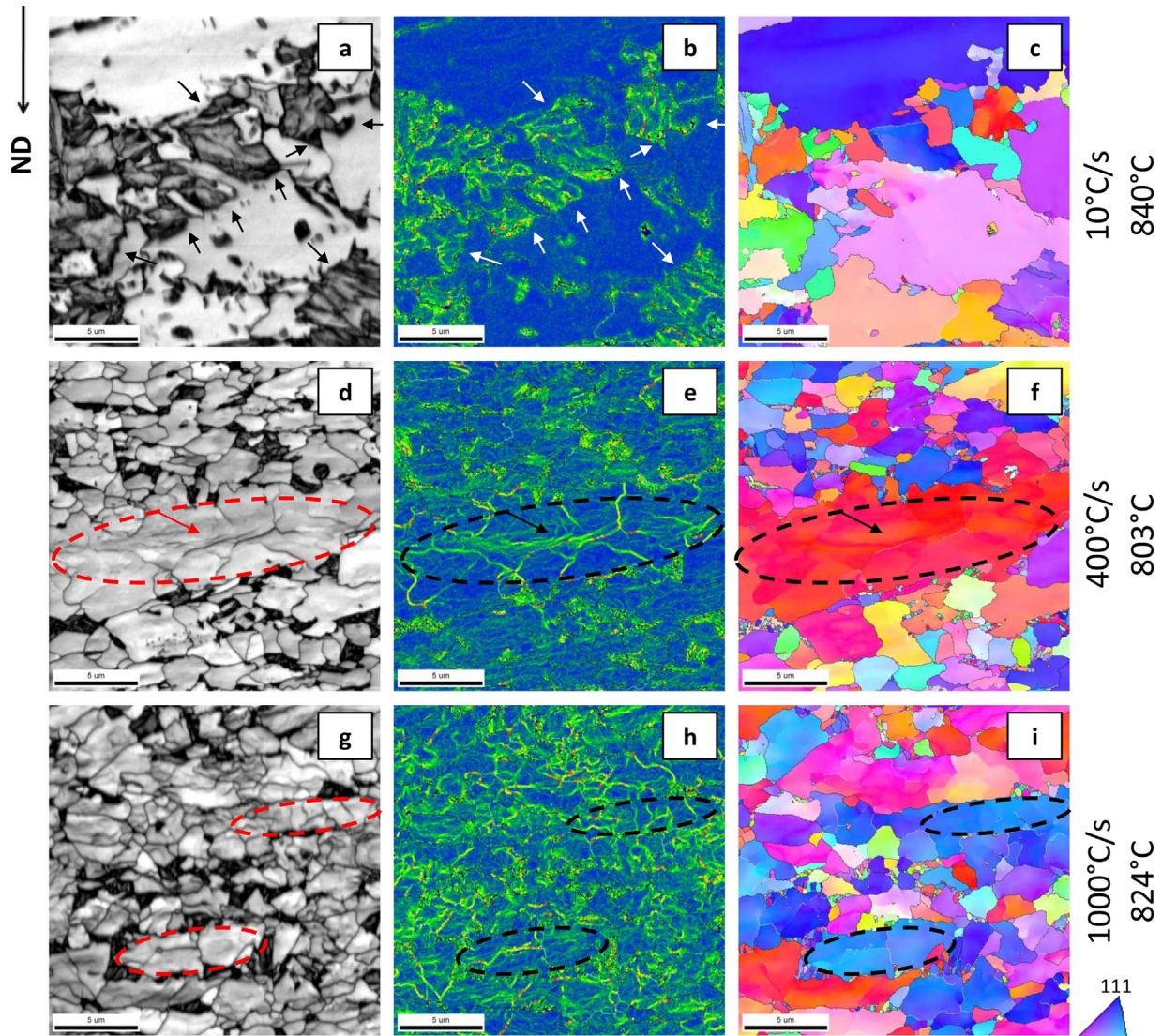


Figure 9. EBSD maps of samples heated treated under the following conditions: $10\text{ }^{\circ}\text{C s}^{-1}$ to $840\text{ }^{\circ}\text{C}$ a–c), $400\text{ }^{\circ}\text{C s}^{-1}$ to $803\text{ }^{\circ}\text{C}$ d–f), and $1000\text{ }^{\circ}\text{C s}^{-1}$ to $824\text{ }^{\circ}\text{C}$ g–i). Images on the left-hand side, center, and right-hand side show IQ (Image Quality), KAM (Kernel Average Misorientation), and IPF (Inverse Pole Figure) maps, respectively. In the IQ maps (cf. **Figure 9a,d,g**), martensite appears as dark-gray zones, whereas ferrite grains are light-gray. Black lines define Misorientation Angles (MA) between 15° and 63° , whereas white lines define MA between 5° and 15° . Step-size 50 nm . Scale bar $5\text{ }\mu\text{m}$.

completion. However, one might expect that several small grains with different orientations (and different colors in the IPF map in **Figure 9f**) will result from GB nucleation of recrystallized ferrite. The grain within the dashed area in **Figure 9d–f** corresponds to a single orientation (although with some small rotations $<5^{\circ}$) due to the fact that the original grain serves as active nucleus for the massive transformation of ferrite. Therefore, in spite that many different grains of austenite might have grown massively toward the deformed ferrite one; since the transformation was incomplete the resulting massive ferrite will inherit the orientation of the deformed grain. It is evident that this is the most efficient ferrite growth mechanism from the thermodynamic and kinetic point of view; the former because it does not require the expenditure of Gibbs free energy

in nucleation of new ferritic grains, and the latter stems in the fact that a grain which is in the growth stage will release the available energy much faster than another grain which must undergo nucleation. Analogous morphologies are found in samples heated at $1000\text{ }^{\circ}\text{C s}^{-1}$ to $824\text{ }^{\circ}\text{C}$ (cf. dashed areas in **Figure 6i**, **9g–i**). In samples heated at $10\text{ }^{\circ}\text{C s}^{-1}$ (cf. **Figure 9a–c**), the almost fully recrystallized ferrite will prevent the formation of the morphology previously described.

5.3. Transformation Products

Upon cooling, the massive transformation of ferrite will continue until the a/γ interface reaches a zone where $X_C^a \neq X_C^{\gamma}$.

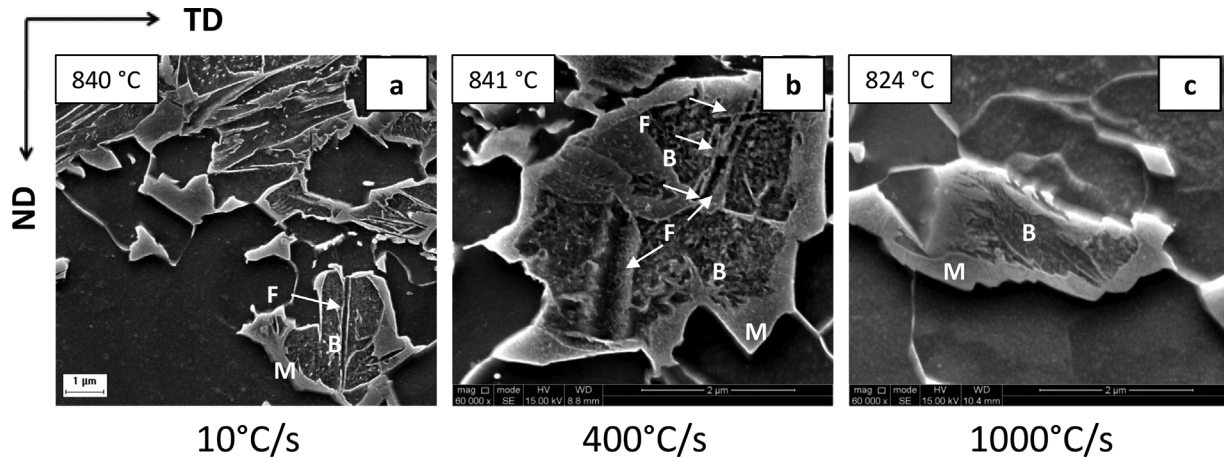


Figure 10. SEM images of samples heated at $10\text{ }^{\circ}\text{C s}^{-1}$ a), $400\text{ }^{\circ}\text{C s}^{-1}$ b), and $1000\text{ }^{\circ}\text{C s}^{-1}$ c). The peak temperatures are indicated in each micrograph.

Further advance of the a/γ interface will be carbon-diffusion controlled, thus producing an accumulation of carbon in front of the moving boundary. The accumulation of carbon combined with the presence of alloying elements as Cr, Mn, and Mo dissolved in austenite will increase the hardenability nearby the a/γ interface. It is thus reasonable to predict the formation of such high-carbon rims of austenite in front of ferrite, even at the quenching rates of the current experiments ($\approx -150\text{ }^{\circ}\text{C s}^{-1}$). Indirect evidence of high carbon content in the austenite (transformed into martensite on quenching) is shown in the IQ and KAM maps of Figure 9a and b. As shown in previous ultrafast experiments,^[10] the IQ value, which is sensitive to the level of distortion of the lattice,^[17] can give a qualitative estimation of the carbon content in martensite. Dark zones in the IQ maps indicate low IQ values and hence larger lattice distortion. Under the assumption that such distortion is caused by the carbon content of martensite, one could reasonably expect that the darker martensitic areas (cf. arrows in Figure 8a) surrounding the less dark martensitic grains represent high carbon martensite surrounding either low carbon martensite or bainite. The corresponding KAM in these high carbon martensitic areas (cf. Figure 8b) display larger values if compared to the center of the grain, which supports the previous statement.

Figure 10 shows (from left to right) high magnification SEM images of samples heated at 10, 400, and $1000\text{ }^{\circ}\text{C s}^{-1}$ (the actual temperatures are on the upper-left corner of each image). The transformation products of austenite quenched from a temperature above A_m^{min} show what seems to be a rim of martensite surrounding a mixture of bainite and Widmanstätten ferrite. The observation of the martensitic rim in SEM images (cf. Figure 10) suggest consistency with the discussion of EBSD-based IQ images (cf. Figure 9) in the previous paragraph. The absence of martensite at the center of the parent austenitic grains can be interpreted as consequence of the partial dissolution of cementite discussed in Section 5.1. The carbon content of austenite, due to the sluggish dissolution of cementite, tends to the composition of the γ/a boundary, i.e., $X_C^{\gamma} \rightarrow X_C^{\gamma/a}$. The carbon content of austenite and, hence, the phase distribution upon is influenced by the undissolved carbides in the

microstructure. The grow of cementite (from undissolved particles, cf. Figure 5d,e) during cooling will take place in parallel to the transformation of ferrite and will draw carbon from the surrounding austenite. There might be a case when the

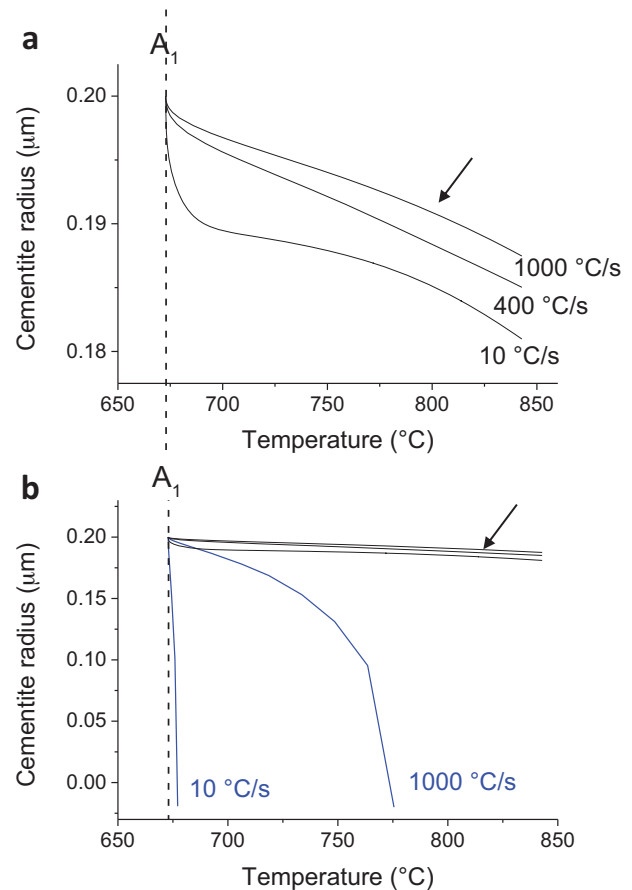


Figure 11. The calculated radius of a cementite particle as function of temperature at different heating rates for a) the studied system and b) the iron-carbon system. Notice the fast dissolution of cementite in b), compared (arrows) to the dissolution in a).

carbon depletion is such that intra-granular Widmanstätten ferrite can nucleate (cf. Figure 6c, g, 10a–c).

5.4. Dictra Calculations

Figure 11 show the calculated cementite dissolution as the variation of its radius (assumed to be of 0.2 μm) with temperature for the three heating rates. The reduction in the radius varies between ≈0.01 and ≈0.02 μm for 10 and 1000 °C s⁻¹, respectively. It is readily observed that the rate of cementite dissolution does not vary significantly with the heating rate in the range of 10–1000 °C s⁻¹. It is therefore expected that the factor $(X_C^\gamma - X_C^{\gamma/\alpha})$ in Equation (1) will not vary significantly within the same range of heating rates, in agreement with the data of Figure 7. A comparison with calculations for Fe–C system (blue curves Figure 11b) show that cementite should fully dissolve slightly above A₁ at 10 °C s⁻¹, whereas at 1000 °C s⁻¹ the full dissolution is accomplished at ≈770 °C. The ‘C’ arrows in Figure 6 show that some cementite particles are not dissolved after heat treatment, which is consistent with the calculations shown in Figure 11.

6. Summary and Conclusions

The microstructure of a low-carbon steel heated at three heating rates and subsequently quenched was studied. Metallographic observation revealed changes in the morphology of austenite, from mainly banded to grain-boundary distribution, at temperatures lower than the predicted average massive limit A_m^{av} . Combined EPMA analyses and thermodynamic calculations revealed that local chemical fluctuations could enable the formation of massive austenite at temperatures well below A_m^{av} , thus explaining the observed microstructure.

The impact of the carbide forming alloying elements on the kinetics of austenite formation is discussed with the aim of a kinetic model. The flux of carbon from cementite to austenite is hindered by the presence of carbide forming alloying elements. Consequently, the flux of carbon in austenite, represented by the term $(X_C^\gamma - X_C^{\gamma/\alpha})$ in (Equation (1)), is small due to the slow dissolution of cementite. The velocity of the γ/α interface is, therefore, slow below A_m . DICTRA calculations shows small variations in the fraction of dissolved cementite in Cr, Mn, and Mo alloyed cementite as the heating rate is increased.

A unique microstructural feature resulting from the massive formation of austenite and the subsequent massive transformation of ferrite in cold-rolled microstructure it is reported for the first time. Metallographic and EBSD observations are discussed in the light of the existing mechanism of phase transformation under ultrafast heating rates.

It is suggested that the microstructure consisting of a mixture of Widmanstätten ferrite and bainite surrounded by a rim of martensite results from the presence of carbon gradients in austenite. The relatively low carbon austenite is enriched due to

the advance of ferrite upon cooling, thereby producing the observed martensitic rim.

Acknowledgements

The authors are thankful to prof. J. Sietsma from TUDelft for kindly providing the facilities for the Dilatometry and Gleeble experiments. F. M. Castro Cerda gratefully acknowledges the support of the Chilean Government in the form of the CONICYT-PCHA/Doctorado Nacional/2013 Ph. D. grant, and of University of Santiago de Chile through the project DESEMPEÑO N°25 - Project Code 1555LD.

This manuscript was modified after first online publication.

Conflict of Interest

The authors declare no conflict of interest.

Keywords

Austenite, Massive, Segregation, Steel, Ultrafast heating

Received: February 10, 2018

Revised: March 9, 2018

Published online: April 3, 2018

- [1] M. J. Bibby, J. G. Parr, *J. Iron Steel Inst. Iron Steel Inst.* **1964**, *202*, 100.
- [2] N. N. Lipchin, T. G. Kryukova, N. L. Oslon, *Metalloved. Term. Obrab. Met.* **1964**, *8*, 5.
- [3] W. I. Haworth, J. G. Parr, *Trans. ASM* **1965**, *58*, 476.
- [4] K. J. Albutt, S. Garber, *J. Iron Steel Inst.* **1966**, *204*, 1217.
- [5] G. E. Abrosimova, G. I. Kohanchik, A. M. Markov, A. V. Serebryakov, *Scr. Metall.* **1979**, *13*, 531.
- [6] Y. Y. Meshkov, E. V. Pereloma, *Phase Transformations in Steels*, Vol. 1 (Eds: E. Pereloma, D. V Edmonds), Woodhead Publishing Series in Metals and Surface Engineering; Woodhead Publishing, Cambridge, UK **2012**, pp. 581–618.
- [7] V. N. Gridnev, V. I. Trefilov, *Dokl. Akad. Nauk SSS* **1954**, *95*, 741.
- [8] J. Rödel, H. J. Spies, *Surf. Eng.* **1996**, *12*, 8.
- [9] M. Enomoto, K. Hayashi, *J. Mater. Sci.* **2015**, *50*, 6786.
- [10] F. M. Castro Cerda, I. Sabirov, C. Goulas, J. Sietsma, A. Monsalve, R. H. Petrov, *Mater. Des.* **2017**, *116*, 448.
- [11] S. Papaefthymiou, C. Goulas, F. M. Castro Cerda, N. Geerlofs, R. Petrov, *Steel Res. Int.* **2017**, *88*. <https://onlinelibrary.wiley.com/action/showCitFormats?doi=10.1002%2Fsrin.201700158>
- [12] J. T. Armstrong, *Electron Probe Quantitation*; Heinrich (Eds: K. F. J. Heinrich, D. E. Newbury), Springer US, Boston, MA **1991**, pp. 261–315.
- [13] A. Oddy, J. Mcdill, L. Karlsson, *Can. Metall. Q.* **1996**, *35*, 275.
- [14] R. C. Dykhuizen, C. V. Robino, G. A. Khorovskiy, *Metall. Mater. Trans. B* **1999**, *30*, 107.
- [15] T. A. Kop, *PhD. Thesis*, TU Delft, **2000**.
- [16] V. I. Savran, *PhD. Thesis*, TU Delft, **2009**.
- [17] R. H. Petrov, L. A. I. Kestens, *Encyclopedia of Iron, Steel, and Their Alloys* (Eds: R. Colás, G. E. Totten), CRC Press, Boca Raton, FL **2016**, pp. 46–69.
- [18] C. Zener, *Trans. AIME* **1946**, *167*, 550.
- [19] J. O. Andersson, L. Höglund, B. Jönsson, J. Ågren, *Fundamentals and Applications of Ternary Diffusion* (Ed: G.R. Purdy), Proceedings of Metallurgical Society of Canadian Institute of Mining and Metallurgy, Pergamon, Oxford **1990**, pp. 153–163.

- [20] A. Borgenstam, L. Höglund, J. Ågren, A. Engström, *J. Phase Equilib.* **2000**, *21*, 269.
- [21] J. O. Andersson, T. Helander, L. Höglund, P. Shi, B. Sundman, *Calphad* **2002**, *26*, 273.
- [22] F. M. Castro Cerda, C. Goulas, I. Sabirov, S. Papaefthymiou, A. Monsalve, R. H. Petrov, *Mater. Sci. Eng. A* **2016**, *672*, 108.
- [23] F. M. Castro Cerda, B. Schulz, S. Papaefthymiou, A. Artigas, A. Monsalve, R. H. Petrov, *Metals* **2016**, *6*, 321.
- [24] H. Landheer, S. E. Offerman, R. H. Petrov, L. A. I. Kestens, *Acta Mater.* **2009**, *57*, 1486.
- [25] V. I. Savran, S. E. Offerman, J. Sietsma, *Metall. Mater. Trans. A* **2010**, *41*, 583.
- [26] C. Zener, *J. Appl. Phys.* **1949**, *20*, 950.
- [27] M. Hillert, K. Nilsson, L.-E. Torndahl, *J. Iron Steel Inst.* **1971**, *209*, 49.